Received: 13 December 2022 | Revised: 13 June 2023 | Accepted: 10 August 2023

DOI: 10.1002/qj.4564

Quarterly Journal of the Royal Meteorological Society RMetS

RESEARCH ARTICLE

Multistability in a coupled ocean–atmosphere reduced-order model: Nonlinear temperature equations

Oisín Hamilton[1,2] | **Jonathan Demaeyer**[1] | **Stéphane Vannitsem**[1] | **Michel Crucifix**[2]

[1]Climate Dynamics, Royal Meterological Institute of Belgium, Brussels, Belgium

[2]Earth and Life Institute, Université catholique de Louvain, Louvain-la-Neuve, Belgium

Correspondence
Oisín Hamilton, Climate Dynamics, Royal Meterological Institute of Belgium, Uccle, 1180 Brussels, Belgium.
Email: oisin.hamilton@meteo.be

Funding information
Horizon 2020 Framework Programme, Grant/Award Number: 956170

Abstract

Multistabilities in the ocean–atmosphere flow were found in a reduced-order ocean–atmosphere coupled model, by solving the nonlinear temperature equations numerically. In this article, we explain how the full nonlinear Stefan–Bolzmann law was implemented numerically and the resulting change to the system dynamics was compared with the original model where these terms were linearised. Multiple stable solutions were found that display distinct ocean–atmosphere flows, as well as different Lyapunov stability properties. In addition, distinct low-frequency variability (LFV) behaviour was observed in multiple attractors. We investigated the impact on these solutions of changing the magnitude of the ocean–atmospheric coupling, as well as the atmospheric emissivity, to simulate an increasing greenhouse effect. Where multistabilities exist for fixed parameters, the possibility for tipping between solutions was investigated, but tipping did not occur in this version of the model where there is a constant solar forcing. This study was undertaken using a reduced-order coupled quasigeostrophic ocean–atmosphere model.

KEYWORDS

coupled ocean–atmosphere model, low-frequency variability, temperature multistabilities

1 | INTRODUCTION

Due to nonlinear processes in the climate system, a global temperature increase could lead to tipping points, causing rapid or irreversible changes to the climate (Lenton *et al.*, 2008). In the North Atlantic, the jet stream has been identified as a potential tipping element (Steffen *et al.*, 2018; Armstrong McKay *et al.*, 2022), potentially causing long-term climate patterns to be fundamentally altered. Low-frequency variability (LFV) describes climate processes that vary slowly on interannual to multidecadal timescales. An example of LFV is the North Atlantic Oscillation (NAO), which is the sea-surface pressure difference between the subtropical and subpolar gyres. Accurate

Abbreviations: AMOC, Atlantic meridional overturning circulation; CLV, covariant Lyapunov vector; DE, dynamic equilibria; LFV, low-frequency variability; LLE, largest Lyapunov exponent; LM, linear model; MAOOAM, modular arbitrary order ocean–atmosphere model; NAO, North Atlantic oscillation; ODE, ordinary differential equation; PDE, partial differential equation; qgs, quasigeostrophic spectral.

modelling of LFV could also help extend the typical two-week weather forecast horizon, which is caused by the sensitivity to initial conditions, in the midlatitudes.

Potential mechanisms for LFV in the midlatitudes include coupling of the ocean with the atmosphere, where temperature, wind stresses, and moisture are transferred from one to another (Holton, 2004). This coupling has been observed in data (Czaja and Marshall, 2001; Wu and Liu, 2005; Årthun *et al.*, 2021). Studies have attempted to reproduce this LFV using models of varying complexity. In this article we focus on modelling LFV using reduced-order dynamical models, and the impacts of linearisations on these dynamics. These models purposely sacrifice the required complexity to model the real climate accurately, and instead focus on the minimum set of conditions necessary to generate a qualitatively similar variability.

Simplifying atmospheric models began with (Lorenz, 1963) and (Veronis, 1963) with reduction of the quasigeostrophic equations using a harsh spectral truncation and removal of small-scale processes. These simplified the governing equations to allow for multiple solutions to be found explicitly. (Charney and DeVore, 1979) developed a land–atmosphere model, using a two-layer quasigeostrophic atmosphere (adapting the one-layer model of Egger (1978)), with a simple topography. The forcing of the zonal flow over topography led to multiple stable equilibria or distinct atmospheric flows, and they believed it was small-scale perturbations or baroclinic instability that caused transitions between solutions.

This claim was analysed by Charney and Straus (1980), who found that the transitions were caused by baroclinic instability instead of zonal flow perturbations when using a baroclinic model. Reinhold and Pierrehumbert (1982) increased the zonal resolution of this model to represent the synoptic-scale baroclinic instability better. They found that the atmospheric flow oscillated between two regimes, but these were not in the region of the equilibria. They conclude that understanding the overall variability in the climate system requires understanding the behaviour of these "regime equilibria". Further work has been undertaken to understand further the multiple regimes present in these systems, to investigate bifurcations (Legras and Ghil, 1985), and to show that these multiple attractors are resilient to the presence of noise (Itoh and Kimoto, 1996).

Studies have investigated the role of the ocean dynamics on LFV in the ocean (Chen and Dewar, 1993). Weng and Neelin (1998); Cessi (2000) implemented coupled versions of similar ocean models where the zonal wind was in turn impacted by ocean temperature gradients. Such studies found that the wind forcing was capable of generating LFV from the baroclinic exchange between gyres, as well as interdecadal modes. LFV was also found in more complex ocean models (Dewar, 2001; Nauw and Dijkstra, 2001; Spydell and Cessi, 2003; Pierini, 2011). These studies included a greater number of quasigeostrophic layers in the ocean models, and found that the intrinsic variability in the solutions comes from gyre modes. Together, these studies showed that intrinsic ocean modes could be sources of LFV in the coupled ocean–atmosphere system, through time separation in heat transfers or ocean gyres generated by wind stresses.

Models using more complex atmospheres coupled to the ocean were developed to study LFV further (Goodman and Marshall, 1999; Ferreira *et al.*, 2001). These studies used a linearised version of the two-layer model introduced in (Charney and Straus, 1980) and a quasigeostrophic two-layer ocean, coupled through thermal and stress forcings. They found analytically that such models contain coupled modes, which were broadly consistent with the NAO, created and maintained by atmospheric Rossby waves moving over sea temperature anomalies. van der Avoird *et al.* (2002) showed that the coupling strength in such models can dictate the presence and strength of coupled modes and alters the behaviour of LFV. However, due to a discrepancy between the NAO variability and the behaviour of the LFV in this model, they concluded that the model was likely missing key dynamics or that the coupled modes play no role in the observed variability. Further work was undertaken to understand the impact of the Atlantic gyre system (Kravtsov and Robertson, 2002), the sensitivity to nonlinear dynamics and interactions between the layers (Kravtsov *et al.*, 2006), and the impacts of ocean eddies on the variability (Berloff *et al.*, 2007).

Multiple attractors in the coupled ocean–atmosphere system have been found in more complex models. Saravanan and Mc Williams (1995) modelled the atmosphere and ocean with the primitive equations and Boussinesq equations, respectively, over a greatly simplified land–ocean base. This model presented multiple coupled attractors as well as coupled LFV. The authors studied the impacts of increasing CO_2 in the model by altering the longwave radiation leaving the greybody atmosphere. They found that as CO_2 was increased the solutions seemed to collapse to a single attractor, due to the weakened jet stream and ocean overturning.

Lorenz (1984) also developed a coupled ocean–atmosphere model based on the primitive equations for the atmosphere and a heat bath (slab) for the ocean. Using a fully nonlinear energy-balance scheme, he was able to show the presence of attractors at different mean temperatures. This model was then extended by Nese and Dutton (1993) in order to incorporate quasigeostrophic transport in the ocean. Hogg *et al.* (2006) (following from (Hogg *et al.*, 2003)) used an intermediate-complexity model to

investigate the impact of ocean temperatures on LFV. They found that the ocean heat flux modified the behaviour and period of the existing LFV in the atmosphere, but was not the cause of the variability.

These previous works have provided considerable hints on the development of multiple solutions in atmospheric and climate models, together with the possibility of the emergence of LFV. These studies, however, have shown limitations in terms of configuration flexibility and modularity. To alleviate these limitations and provide a framework to investigate the emergence of coupled LFV modes, the Modular Arbitrary Order Ocean–Atmosphere Model (MAOOAM: (De Cruz *et al.*, 2016; Demaeyer *et al.*, 2020) was developed. To do this, the atmosphere model of Charney and Straus (1980) was coupled with the simplified ocean model of Pierini (2011), as described in Vannitsem and De Cruz (2014). It was shown that the combination of an energy-balance model and a wind-stress ocean forcing was essential in the development of LFV (Vannitsem *et al.*, 2015). This model thus reduces the complexity of previous atmosphere–ocean coupled models, provides a flexible framework in which the domain size and the number of retained modes can be easily modified, and produces coupled LFV while retaining a good representation of the large-scale ocean and dry atmosphere dynamics.

A source of nonlinearity in this model comes from the longwave radiation modelled using the Stefan–Boltzmann law ($\sigma_B T^4$, where σ_B is the Stefan–Boltzmann constant). In the MAOOAM model, the quartic radiation terms are linearised to simplify the numerical integration. This linearisation is justified, as the perturbations in temperature are small relative to the average temperatures (De Cruz *et al.*, 2016). However, this linearisation removes the possibility of nonlinear interactions from the temperature terms.

We will show that relaxing the linearisation leads to multiple stable flow patterns in the atmosphere and ocean for certain parameter values. These flow patterns are qualitatively distinct and result in multiple average temperatures for the same model parameters. The MAOOAM model is well suited to studying this, due to its simplified dynamics, while retaining nonlinear longwave radiation terms for both the ocean and atmosphere layers. Section 2 describes the reduced-order model used in this study and Section 2.3 describes the modifications made to remove the requirement of linearising the temperature equations. This section also gives a description of the model configurations used in this study. The results are split into three sections, where we first look at the results from altering the ocean–atmosphere coupling (Section 3.1), then the impact of atmospheric emissivity (Section 3.2). We also look at the impact of altering these two parameters on the stability and predictability of the system. In Section 3.3 we present the impact of model resolution on the previous results. Section 4 summarises the main results and discusses the general implications of these findings.

2 | QGS MODEL

2.1 | Model description

The quasigeostrophic spectral (qgs) model (Demaeyer *et al.*, 2020) is a framework of reduced-order mid-latitude climate models with different model configurations available. In the present work, we use the ocean–atmosphere model version where the atmospheric flow is obtained from a two-layer quasigeostrophic flow defined on a β plane (Reinhold and Pierrehumbert, 1982). Similarly, the ocean stream functions are modelled using a quasigeostrophic shallow-water model with a rigid lid (Pierini, 2011). The thermodynamic equations for the atmosphere and ocean temperatures are derived using an energy-balance scheme similar to the one proposed by Barsugli and Battisti (1998). The coupled ocean–atmosphere scheme used here was first introduced by (Vannitsem *et al.*, 2015). The atmospheric variables are coupled through wind stress to the oceanic ones, driving the ocean circulation, which transports heat in the ocean. The ocean transfers heat with the atmosphere through radiative and direct heat coupling, which in turn impacts the atmospheric flow.

In this study we imposed a closed ocean basis (no-flux boundary conditions on all boundaries) and a channel atmosphere (no-flux boundary conditions on the north and south boundaries and periodic boundary conditions at the west and east). We describe how these boundary conditions are implemented in Section 2.2. This version of the model with a closed ocean basin coupled to an atmosphere is called MAOOAM (De Cruz *et al.*, 2016).

The governing partial differential equations (PDEs) for the atmosphere barotropic ψ_a and baroclinic θ_a stream functions and ocean stream functions ψ_o are given as

$$\frac{\partial}{\partial t}\left(\nabla^2\psi_a\right) + J\left(\psi_a, \nabla^2\psi_a\right) + J\left(\theta_a, \nabla^2\theta_a\right) + \beta\frac{\partial\psi_a}{\partial x} = -\frac{k_d}{2}\nabla^2(\psi_a - \theta_a - \psi_o), \tag{1}$$

$$\frac{\partial}{\partial t}\left(\nabla^2\theta_a\right) + J\left(\psi_a, \nabla^2\theta_a\right) + J\left(\theta_a, \nabla^2\psi_a\right) + \beta\frac{\partial\theta_a}{\partial x} = -2k_d'\nabla^2\theta_a + \frac{k_d}{2}\nabla^2(\psi_a - \theta_a - \psi_o) + \frac{f_0}{\Delta p}\omega, \tag{2}$$

$$\frac{\partial}{\partial t}\left(\nabla^2\psi_o - \frac{\psi_o}{L_R^2}\right) + J\left(\psi_o, \nabla^2\psi_o\right) + \beta\frac{\partial\psi_o}{\partial x} = -r\nabla^2\psi_o + d\nabla^2(\psi_a - \theta_a - \psi_o), \tag{3}$$

where ω are the vertical velocities.

The ocean and atmosphere temperatures are derived from an energy-balance model:

$$\gamma_a\left(\frac{\partial T_a}{\partial t}+J(\psi_a,T_a)-\sigma\omega\frac{p}{R}\right) = -\lambda(T_a-T_o)+\varepsilon\sigma_B T_o^4-\varepsilon\sigma_B T_a^4+R_a, \quad (4)$$

$$\gamma_o\left(\frac{\partial T_o}{\partial t}+J(\psi_o,T_o)\right) = -\lambda(T_o-T_a)-\sigma_B T_o^4+\varepsilon\sigma_B T_a^4+R_o, \quad (5)$$

where T_a and T_o are the atmosphere and ocean temperatures, γ_a and γ_o are the heat capacities of the atmosphere and ocean, σ is the static stability of the atmosphere (assumed constant), σ_B is the Stefan–Boltzmann constant, R_a and R_o are the incoming solar radiation absorbed by the atmosphere and ocean, and ε is the atmospheric emissivity.

To reduce the number of variables, the atmosphere temperature variable T_a is related to the baroclinic stream functions using the hydrostatic balance in pressure coordinates and the ideal gas law, providing the relationship $T_a = 2f_0\theta_a/R$.

2.2 | Numerical solution

The differential equations are projected onto basis modes, a procedure also known as a Galerkin expansion. The basis modes are chosen to ensure that the boundary conditions described in the previous section are satisfied. This is done by stipulating that $\phi_i(x,y)=0$ for points (x,y) on the boundary, $\partial F_i(x,y)/\partial x = 0$ for x on the boundary, and $F_i(x,y)=0$ for y on the boundary. In this study we use 10 basis modes for the atmosphere and eight for the ocean, as in Vannitsem (2017). These are set on a domain of $x\in[0,2\pi]$, $y\in[0,\pi]$. The atmosphere F_i and ocean ϕ_i modes are given below:

$$\begin{aligned}
F_1 &= \sqrt{2}\cos(y), & &\\
F_2 &= 2\cos(nx)\sin(y), & \phi_1 &= 2\sin(nx/2)\sin(y),\\
F_3 &= 2\sin(nx)\sin(y), & \phi_2 &= 2\sin(nx/2)\sin(2y),\\
F_4 &= \sqrt{2}\cos(2y), & \phi_3 &= 2\sin(nx/2)\sin(3y),\\
F_5 &= 2\cos(nx)\sin(2y), & \phi_4 &= 2\sin(nx/2)\sin(4y),\\
F_6 &= 2\sin(nx)\sin(2y), & \phi_5 &= 2\sin(nx)\sin(y),\\
F_7 &= 2\cos(2nx)\sin(y), & \phi_6 &= 2\sin(nx)\sin(2y),\\
F_8 &= 2\sin(2nx)\sin(y), & \phi_7 &= 2\sin(nx)\sin(3y),\\
F_9 &= 2\cos(2nx)\sin(2y), & \phi_8 &= 2\sin(nx)\sin(4y),\\
F_{10} &= 2\sin(2nx)\sin(2y). & &
\end{aligned} \quad (6)$$

Three basis modes are of particular interest as they have real world analogies.

- $F_1(x,y)=\sqrt{2}\cos(y)$ represents the solar insolation imbalance between the north and south.
- $\phi_1(x,y)=2\sin(x/2)\sin(y)$ represents average temperature fluctuations in the ocean.
- $\phi_2(x,y)=2\sin(x/2)\sin(2y)$ is the double gyre, orientated so the peak is to either the north or the south of the trough. This loosely approximates the NAO, which is defined by the difference in surface-pressure anomalies between northern and southern locations (often the Azores and Iceland: (Hurrell *et al.*, 2003). The prevailing clockwise winds around the Azores high and the counterclockwise winds around the northern low pressure can be broadly simulated by projecting the atmospheric stream function anomalies on this mode, thus simulating the impact on the wind and heat transport caused by the NAO.

The model variables are expanded using the basis modes. In previous studies using such energy-balance models, the temperature variables in the model are linearised around an equilibrium temperature fixed in time: $T(t,x,y)=T_0+\delta T(t,x,y)$, to remove the quartic terms $\sigma_B T^4$ (Vannitsem *et al.*, 2015). This resulted in the temperatures being expressed as

$$\begin{aligned}
T_a(t,x,y) &= T_{a,0}+\delta T_a(t,x,y) = T_{a,0}+\sum_{i=1}^{10}\delta T_{a,i}(t)F_i(x,y),\\
T_o(t,x,y) &= T_{o,0}+\delta T_o(t,x,y) = T_{o,0}+\sum_{i=1}^{8}\delta T_{o,i}(t)\phi_i(x,y).
\end{aligned} \quad (7)$$

The PDEs introduced in Equations 4 and 5 are then projected onto these basis modes, using the inner product:

$$\langle f,g\rangle = \frac{n}{2\pi^2}\int_0^{\pi}\int_0^{2\pi/n} f(x,y)g(x,y)\,dx\,dy. \quad (8)$$

This leads to 20 ordinary differential equations (ODEs) for the atmospheric stream functions: 10 for the barotropic and 10 for the baroclinic stream functions. In addition there are 16 ODEs in the ocean, eight for the barotropic stream functions and eight for the temperature anomaly. This leads to a total of 36 ODEs describing the model.

2.3 | Model modifications

This study focuses on the change in the system dynamics from altering the way radiation terms in the temperature equations of the MAOOAM model are solved numerically. This requires the reference temperature $T_{a,0}$ and $T_{o,0}$ to be time-varying quantities in the expansions shown in Equation 7. Therefore, to allow the average temperature

across the atmosphere and ocean to change dynamically with time, we introduced two new basis modes, corresponding to constant spatial modes: $F_0(x,y) = 1$ and $\phi_0(x,y) = 1$. These modes were added to the list of basis modes that were introduced in Section 2.2:

$$\begin{aligned} F_0 &= 1, & \phi_0 &= 1, \\ F_1 &= \sqrt{2}\cos(y), & \phi_1 &= 2\sin(nx/2)\sin(y), \\ F_2 &= 2\cos(nx)\sin(y), & \phi_2 &= 2\sin(nx/2)\sin(2y), \\ &\vdots & &\vdots \end{aligned} \tag{9}$$

These additional basis modes now allow the expansions, shown in Equation 7, to be given as $T_o(t,x,y) = \sum_{i=0}^{8} T_{o,i}(t)\phi(x,y)$, and similarly for the atmosphere.

Only the temperature equations are projected onto these additional basis modes, as these are the variables linearised in the original MAOOAM model. This means that we still have 10 ODEs for the atmospheric barotropic stream functions and eight ODEs for the oceanic barotropic stream functions. We obtain an additional ODE for the atmospheric baroclinic stream function (as this variable replaces the atmospheric temperature variables) and for the ocean temperature. This increases the total number of ODEs describing the system to 38.

We now introduce the two modified versions of the model that are used in the current study.

Dynamic equilibria: this version of the model includes the same linearisation as the linearised version of the model, but the equilibrium temperature is dependent on time: $T(t,x,y) = T_0(t) + \delta T(t,x,y)$. We will refer to this version as DE.

Nonlinear T4: This version does not involve the linearisation of the Stefan–Boltzmann law terms and the equations are projected directly onto the basis modes. This retains the quartic radiation terms. We will refer to this version of the model as T4.

This results in three model versions:

- linear model (LM);
- dynamic equilibria (DE);
- nonlinear (T4).

More information about how these modifications were made can be found in the model manual (Demaeyer *et al.*, 2022). See also the Supporting Information.

3 | RESULTS

The results section is split into two main parts. First we describe the system dynamics when the ocean atmosphere coupling is altered and second we alter the atmospheric emissivity. We focus on values of these parameters that result in multiple distinct ocean–atmosphere flows, which are described by distinct attractors. Multiple stationary attractors, for given parameter values, provide the possibility for model solutions to transition from one attractor to another, provided appropriate forcing is imposed. Such transitions between attractors could represent tipping points or abrupt changes or switching in flows. We are particularly interested in flows that present LFV, generated by the coupling between ocean and atmosphere variables, due to the increased predictability of the system dynamics that these solutions provide.

3.1 | Ocean–atmosphere coupling

This section presents the results where the magnitude of ocean–atmosphere coupling is varied for the three model versions. Increasing the ocean–atmosphere coupling has the effect of increasing the heat transfer between the ocean and the atmosphere. This reduces the ocean temperature (which has a higher equilibrium temperature than the atmosphere) and increases the atmospheric temperature, which has an impact on the baroclinic stream functions. The ocean temperature anomalies cause uneven temperature exchanges in the atmosphere that require the heat energy to be transported by atmospheric winds. At the same time, increasing the ocean–atmosphere coupling increases the friction felt by the atmosphere from the surface wind stresses with the ocean. In turn, this causes the atmospheric wind to have a greater impact on the movement of sea-temperature anomalies. Together, this reduces the fast-moving timescales of the atmosphere through coupling to the ocean, which has a slower timescale relative to the atmosphere.

We alter the ocean–atmosphere coupling C by altering the following parameters: the strength of the ocean–atmosphere coupling d, the ocean–atmosphere friction k_d, the internal atmosphere friction k'_d, and the direct heat transfer between the ocean and atmosphere λ (Vannitsem, 2015). These parameters are controlled using a single friction coefficient C, where the relationship between C and the above parameters is given in Table 1. In this study we focus on values of C that are deemed to be within a realistic range ($C \in [0.008\,\mathrm{kg}\cdot\mathrm{m}^{-2}\cdot\mathrm{s}^{-1}, 0.02\,\mathrm{kg}\cdot\mathrm{m}^{-2}\cdot\mathrm{s}^{-1}]$) for the real-world coupling of ocean and atmosphere (Houghton, 1986; Nese and Dutton, 1993; Vannitsem, 2017).

3.1.1 | State-space probing

The effect of the ocean–atmosphere coupling on the system dynamics was investigated by fixing the coupling

TABLE 1 MAOOAM model parameters used in this study.

Parameter	Value	Description (units)
β	1.62×10^{-11}	The meridional gradient of the Coriolis parameter at a given latitude ($m^{-1} \cdot s^{-1}$)
f_0	1.032×10^{4}	Coriolis parameter (s^{-1})
k_d	$gC/\Delta p$	Atmosphere–surface friction (s^{-1})
k'_d	$gC/\Delta p$	Internal atmosphere friction (s^{-1})
r	1×10^{-7}	Ocean bottom Rayleigh friction (s^{-1})
L_R	1.9934×10^{4}	Reduced Rossby deformation radius
h	136.5	Depth of the ocean layer (m)
d	$C/(\rho_o h)$	Coefficient of mechanical ocean–atmosphere coupling (s^{-1})
γ_a	1×10^{7}	Specific heat capacity of the atmosphere ($J \cdot m^{-2} \cdot K$)
γ_o	5.46×10^{8}	Specific heat capacity of the ocean ($J \cdot m^{-2} \cdot K^{-1}$)
σ	0.2	Static stability of the atmosphere
λ	$1004C$	Sensible and turbulent heat exchange between ocean and atmosphere ($W \cdot m^{-2} \cdot K^{-1}$)
R	287.058	Gas constant in dry air ($J \cdot kg^{-1} \cdot K^{-1}$)
σ_B	5.67×10^{-8}	Stefan–Boltzmann constant ($J \cdot m^{-2} \cdot s^{-1} \cdot K^{-4}$)

Note: Here C is a variable that we alter to investigate the impact of the ocean–atmosphere coupling. As in Charney and Straus (1980), we assume $k' = k_d$, and as in Vannitsem *et al.* (2015) that gravity $g = 10\,m \cdot s^{-2}$.

value C and running many trajectories with random initial conditions. Once these trajectories had appeared to settle onto an attractor, the initial transient section of the trajectories was discarded and we continued to run the trajectories for long run times (1×10^7 model days). This was done to ensure that the attractors remain attracting and trajectories remain on the attractor. For these experiments, the atmosphere emissivity was set to $\varepsilon = 0.7$ as the model default (De Cruz *et al.*, 2016). This process was repeated for different values of C.

The average temperatures of the ocean and atmosphere were calculated by projecting the trajectories that were embedded within an attractor onto the basis modes to obtain the temperature profiles for each time step. We then took the average across the spatial domain to obtain a single average temperature for each time step. Finally we took the average across time to obtain a single temperature, which represents the average temperature associated with a given attractor. This process is shown for the temperature of the ocean, with a similar process taken to calculate the average atmospheric temperatures:

$$\langle T_o(t)\rangle_{\text{space, time}} = \frac{1}{n_\tau n_x n_y} \sum_{\tau=0}^{n_\tau} \sum_{i=0}^{n_x} \sum_{j=0}^{n_y} \sum_{k=0}^{n_o} T_{o,k}(t_\tau)\phi_k(x_i, y_j),$$

where n_o are the number of ocean modes, n_x and n_y are the number of spatial grid points being averaged across, and n_τ is the number of time steps in the numerical solution.

3.1.2 | Multistabilities in temperature–C

The average spatial and temporal temperatures are presented on a temperature–C diagram. These diagrams are not bifurcation diagrams, as we only have information about the attracting branches that we could find using the method described. The resulting diagrams for the average atmosphere and ocean temperatures, where the value of the ocean–atmosphere coupling is altered, are shown in Figure 1. In this figure, the branches are colour-coded depending on the qualitative behaviour of the attractor. The figures show there are two intervals of C where there are multistabilities in the temperature. These intervals are approximately $C \in [0.008\,kg \cdot m^{-2} \cdot s^{-1}, 0.009\,kg \cdot m^{-2} \cdot s^{-1}]$ and $C \in [0.012\,kg \cdot m^{-2} \cdot s^{-1}, 0.0127\,kg \cdot m^{-2} \cdot s^{-1}]$. The diagrams also show that a single attracting branch exists that bridges the two intervals (shown in blue (and as dots)). We plot the results of the dynamic equilibria (DE) and nonlinear (T4) model runs on the same plot.

We found two differences between the T4 and DE runs. The first is that the difference in average temperatures between the attracting branches in the DE runs is smaller than in the T4 runs. The small temperature differences between the attractors in the DE runs occurs due to the zeroth-order temperature equations that control the equilibrium temperature ($T_{a,0}$, $T_{o,0}$) having only one real stable solution. This means that the difference in average temperatures in the stationary dynamics is caused by only higher-order terms. In the T4 model, there are additional

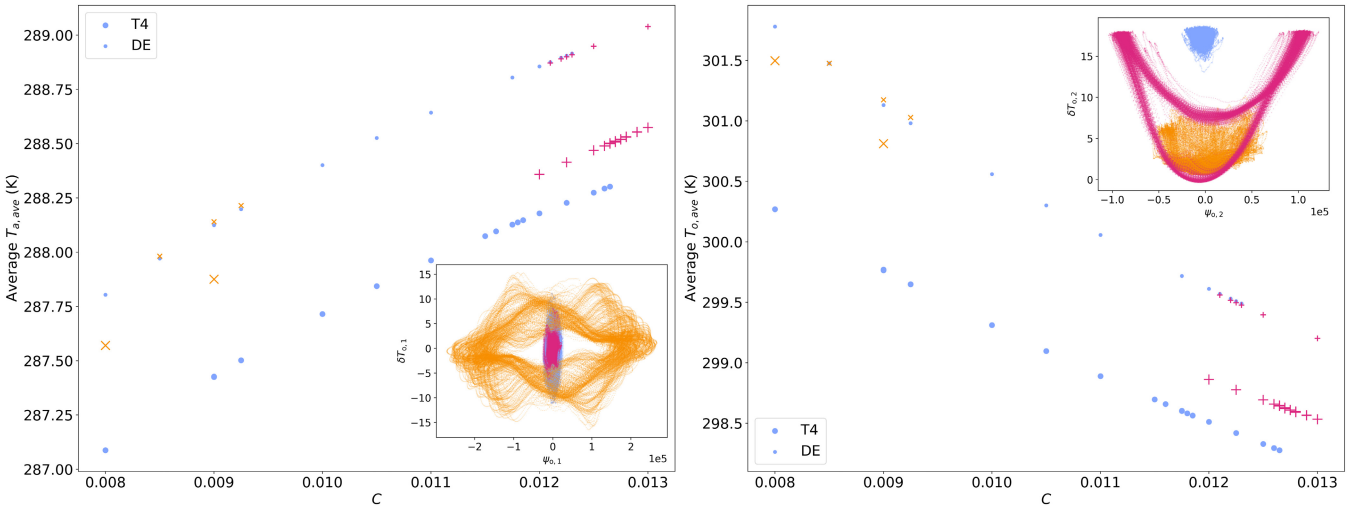

FIGURE 1 Temperature–C diagrams for the averaged atmosphere (left) and ocean (right) temperatures for the DE model (small symbols) and the T4 mode (large symbols) of the attractors. The branches were colour-coded by investigating the behaviour of each attractor qualitatively. The attractors are projected onto the planes $(\psi_{o,1}, T_{o,1})$ (left) and $(\psi_{o,2}, T_{o,2})$ (right), to display how the behaviour differs between the three attractors. The projection of the orange (x) attractor is shown for $C = 0.009\,\mathrm{kg}\cdot\mathrm{m}^{-2}\cdot\mathrm{s}^{-1}$ and the other two projections (blue (dots) and pink (+)) of the attractors are shown for $C = 0.0125\,\mathrm{kg}\cdot\mathrm{m}^{-2}\cdot\mathrm{s}^{-1}$. [Colour figure can be viewed at wileyonlinelibrary.com]

TABLE 2 Modified longwave radiation terms of the tensor $v_{i,j,k,l,m} = \langle F_i,\ \phi_j,\ \phi_k,\ \phi_l,\ \phi_m \rangle$.

	Full term	Zeroth-order term
DE model	$T_{o,0}^4 + 4T_{o,0}^3 \sum_{m=1}^{n_o} v_{i,0,0,0,m} T_{o,m}$	$T_{o,0}^4$
T4 model	$\sum_{j,k,l,m=0}^{n_o} v_{i,j,k,l,m} T_{o,j} T_{o,k} T_{o,l} T_{o,m}$	$T_{o,0}^4 + \sum_{j,k,l,m=1}^{n_o} v_{0,j,k,l,m} T_{o,j} T_{o,k} T_{o,l} T_{o,m}$

terms in the zeroth-order temperature equations that result in larger differences between the zeroth-order temperatures. This difference in the equations occurs in the nonlinear longwave radiation terms. These terms of the tensor are shown in Table 2 where we introduce the modified longwave radiation terms of the tensor $v_{i,j,k,l,m} = \langle F_i,\ \phi_j,\ \phi_k,\ \phi_l,\ \phi_m \rangle$.

The second difference between the model runs is that the T4 runs show a wider region of multistability in the interval $C \in [0.012\,\mathrm{kg}\cdot\mathrm{m}^{-2}\cdot\mathrm{s}^{-1}, 0.0127\,\mathrm{kg}\cdot\mathrm{m}^{-2}\cdot\mathrm{s}^{-1}]$. This is again assumed to be a result of higher-order terms interacting in the T4 model equations, when compared with the DE runs, where the linearisation removes the higher-order terms.

To investigate the properties of the attractors in regions of multiple stability, the attractors were projected onto the ocean variables $(\psi_{o,1}, T_{o,1})$ and $(\psi_{o,2}, T_{o,2})$ to visualise the behaviour. Looking at these projections, we can see that there are three qualitatively distinct attractor behaviours, which correspond to three distinct flow behaviours in the ocean. We project all three attractors onto the same figure for comparison (Figure 1), with the orange (shoen as x) attractor shown for $C = 0.009\,\mathrm{kg}\cdot\mathrm{m}^{-2}\cdot\mathrm{s}^{-1}$ and the other two attractors for $C = 0.0125\,\mathrm{kg}\cdot\mathrm{m}^{-2}\cdot\mathrm{s}^{-1}$. In the interval $C \in [0.008\,\mathrm{kg}\cdot\mathrm{m}^{-2}\cdot\mathrm{s}^{-1}, 0.009\,\mathrm{kg}\cdot\mathrm{m}^{-2}\cdot\mathrm{s}^{-1}]$, two attractors exist, where the attractor shown in orange displays LFV with respect to the variables $(\psi_{o,1}, T_{o,1})$. The orange attractor becomes unstable when $C > 0.009\,\mathrm{kg}\cdot\mathrm{m}^{-2}\cdot\mathrm{s}^{-1}$. This multistability has not been found in other studies using the linear MAOOAM model. The LFV in the first ocean modes suggests that the variability in the ocean temperature and stream functions is impacted prominently by the single gyre oscillation in this case.

The pink (shown as +) attractor, which becomes attracting for values $C > 0.012\,\mathrm{kg}\cdot\mathrm{m}^{-2}\cdot\mathrm{s}^{-1}$, presents LFV over the variables $(\psi_{o,2}, T_{o,2})$, signifying that the dynamics of the flow is impacted by the double gyre dynamics. The other attractor (blue, or as dots) present does not show LFV with any of the modes and this signifies that flows associated with this attractor do not present the same LFV or the same ocean dynamics as the other two attractors. The blue attractor disappears for values $C > 0.01275\,\mathrm{kg}\cdot\mathrm{m}^{-2}\cdot\mathrm{s}^{-1}$. This second bifurcation was found in Vannitsem (2017) using the linear version of the model, however the region of multistability in this interval was not found using the linear model. We have conducted long model

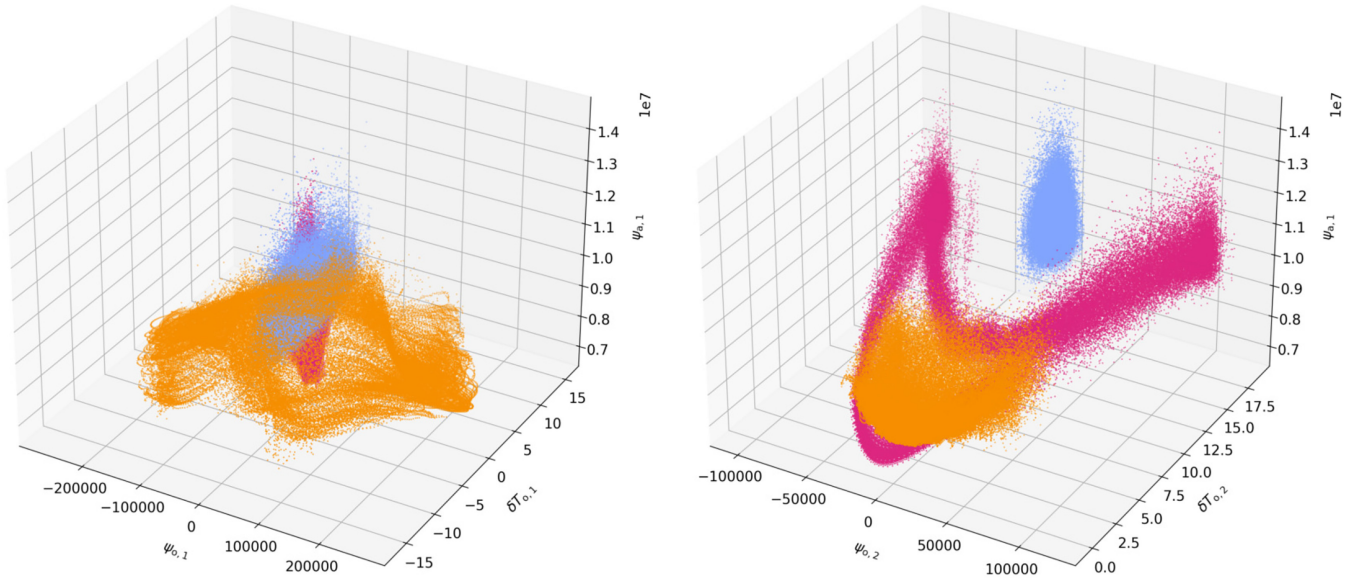

FIGURE 2 The distinct attractors for the T4 runs are projected onto $(\psi_{a,1}, \psi_{o,1}, T_{o,1})$ (left) and $(\psi_{a,1}, \psi_{o,2}, T_{o,2})$ (right), to present the level of ocean–atmosphere coupling. The orange attractor is shown for $C = 0.009\,\mathrm{kg}\cdot\mathrm{m}^{-2}\cdot\mathrm{s}^{-1}$ and the other two attractors are shown for $C = 0.0125\,\mathrm{kg}\cdot\mathrm{m}^{-2}\cdot\mathrm{s}^{-1}$. Here we only present the T4 runs, as the dynamics over these three variables are identical between the T4 and DE model runs. [Colour figure can be viewed at wileyonlinelibrary.com]

runs to ensure the stability of both attractors in this interval and found that both attractors remain stable for at least 3×10^7 model days. This region of multistability was found in both the T4 and DE model runs, however it was found that the region of multistability is extended in the T4 model compared with the DE model.

Following the analysis of (Vannitsem *et al.*, 2015), we project the attractors onto the variables $(\psi_{a,1}, \psi_{o,1}, T_{o,1})$ and $(\psi_{a,1}, \psi_{o,2}, T_{o,2})$ to visualise the degree of ocean–atmosphere coupling in the attractors. In Figure 2 we show all three attractors, for the same values of C as before. In each image there is one attractor that develops around an unstable orbit that varies across all three variables over a decadal timescale. The image displaying $(\psi_{a,1}, \psi_{o,2}, T_{o,2})$ shows that the attractor coloured in pink presents the same oscillating behaviour over the three variables as the attractor found in Vannitsem (2017). In addition, we also recover the attractor found by Vannitsem that does not present LFV (blue, or dots). The novel result here is that we have found an additional attractor (orange, or x), for lower values of C, that also displays LFV in the coupled ocean–atmosphere system, but across the ocean–atmosphere modes $(\psi_{a,1}, \psi_{o,1}, T_{o,1})$.

To visualise the resulting flow in the ocean, given the attractor behaviour, we have created videos showing the ocean stream function and temperature profiles, given the location in the projected 2D state space, which can be found in the Supporting Information. The videos are named based on the colour coding used in the above plots. The attractor coloured in blue (dots) shows a persistent positive value for the $T_{o,2}$ variable, leading to a persistent double gyre temperature anomaly in the ocean temperature. In addition no clear LFV is present in the videos. The pink (+) attractor shows oscillating behaviour over the variables $T_{o,2}$ and $\psi_{o,2}$ with timescales of approximately 70 model years, leading to transitions between a double and quadruple gyre temperature anomaly in the ocean. Similarly, a clear oscillation is seen in the ocean stream function where the most prominent variables oscillate between $\psi_{o,2}$ and $\psi_{o,6}$ over the same time period. Lastly, in the case of the orange (x) attractor, no clear double gyre appears in the ocean temperature profile, and the LFV instead manifests in the first ocean mode $\phi_{o,1}$. This leads to LFV with a timescale of 80–100 model years over the temperature variables $T_{o,1}$, $T_{o,5}$, and $T_{o,7}$.

3.1.3 | Lyapunov stability–C

To analyse the stability properties of the attractors that were found, we calculated their Lyapunov properties, focusing on values of C identified in the previous section where multiple attractors exist. For more details on calculating Lyapunov properties in coupled ocean–atmosphere models, see Vannitsem and Lucarini (2016); Vannitsem (2017); Vannitsem *et al.* (2019); Vannitsem and Duan (2020).

We present the largest Lyapunov exponents (LLE) in Figure 3a, as a function of C, where again there is a multistability present in the two intervals identified. We have

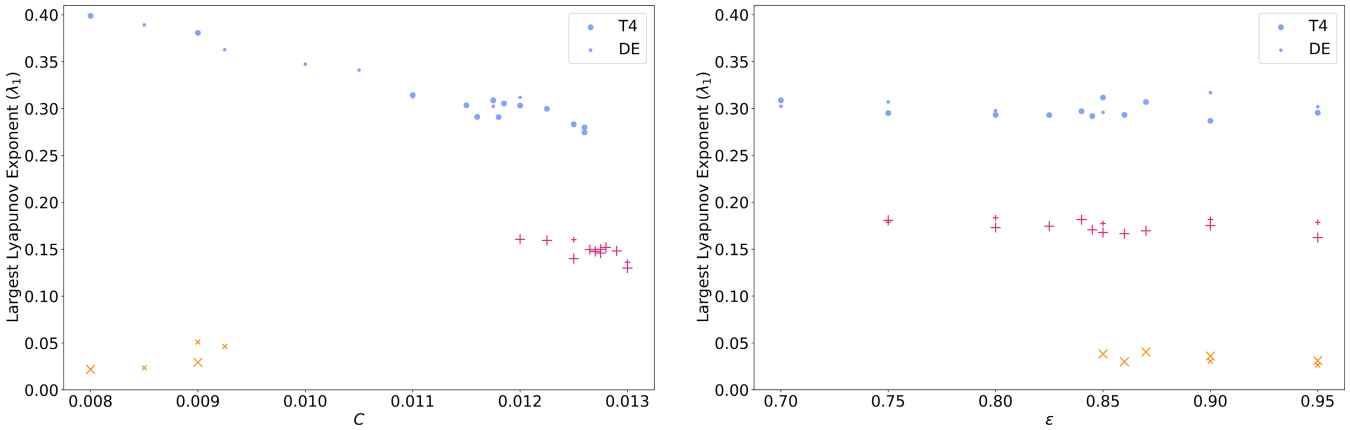

(a) LLE of the DE and T4 model runs, for varying C and $\varepsilon = 0.7$.

(b) LLE of the DE and T4 model runs, for $C = 0.01175 \text{kgm}^{-2}\text{s}^{-1}$ and varying ε.

FIGURE 3 The largest Lyapunov exponents (LLE), shown in days^{-1}, where the results are colour-coded based on the attractor behaviour, as described in Sections 3.1.2 and 3.2.1. [Colour figure can be viewed at wileyonlinelibrary.com]

used the same colour coding as in Section 3.1.2 to display which Lyapunov exponent is associated with which attractor. Approximately, the midlatitudes have a synoptic forecast timescale of less than 2 weeks (Lorenz, 1982), with larger scale process having a larger forecasting time (Lorenz, 1969). At the synoptic scale, this would correspond to LLE of approximately 0.2–0.3 days^{-1}. In the MAOOAM model there is a general decrease in the magnitude of the LLEs as C increases, due to the increase in coupling between the ocean and atmosphere, resulting in flow instabilities from the atmospheric dynamics being reduced (Vannitsem, 2017). However, it is clear that the orange (x) branch displays significantly smaller LLEs than the other two branches for relatively small values of C. Other studies have shown that for low values of C the magnitudes of LLEs do decrease (Vannitsem, 2017); however, this was observed for values $C \leq 0.0015\,\text{kg} \cdot \text{m}^{-2} \cdot \text{s}^{-1}$, and we did not carry out runs for values of C this low due to these ocean–atmospheric coupling values being unrealistic in the real Earth system.

In Figure 4a we present the Lyapunov spectra of the three distinct attractors identified while varying the level of ocean–atmosphere coupling. The figure shows that the two attractors at $C = 0.0125\,\text{kg} \cdot \text{m}^{-2} \cdot \text{s}^{-1}$ (blue (dots) and pink (+)) both have 18 near-zero Lyapunov exponents, 17 negative exponents, and three positive exponents. However, the positive Lyapunov exponents are approximately double in one of the attractors compared with the other, showing that the rate of divergence of initial conditions will be much greater in the blue attractor. The novel attractor found in this study (orange, x) presents significantly smaller magnitude positive Lyapunov exponents than the other attractors, and has a lower number of near-zero Lyapunov exponents, implying that the attractor exists on a lower dimensional chaotic manifold than the other attractors. The smaller positive magnitude Lyapunov exponents for two of the three attractors occur due to these attractors existing around unstable periodic orbits that produce the LFV on decadal timescales and therefore increase the predictability.

The extent to which coupling between the ocean and atmosphere is responsible for the LFV can be visualised using the variance of covariant Lyapunov vectors (CLVs: (Vannitsem and Lucarini, 2016). The CLVs provide a covariant basis of the tangent linear space of the system. In other words, the CLVs are vectors that form a basis and remain covariant with the flow, unlike forwards or backwards Lyapunov vectors (Kuptsov and Parlitz, 2012). Each covariant Lyapunov vector is stretched by the system dynamics by the corresponding local Lyapunov exponent. Each CLV is made up of 38 components, one for every variable of the system. The CLVs were calculated at each time step, and we took the variance of each of the 38 vector components across time for each of the 38 vectors. The variance measures the variability of the CLV component in the direction of a given variable. Variables from the atmosphere and ocean both have high variance for the same CLV index, implying that these variables are interacting or influencing each other. Therefore variables that are coupled with one another will present higher variance for the same CLV index (horizontal rows on the diagram). This allows us to visualise which variables are coupled and have a greater impact on the system dynamics. In Figure 5 we present a heatmap of the variance ($\log_{10}$ scale) for the three distinct attractors of Figure 1. These plots show the CLV index on the y-axis and the

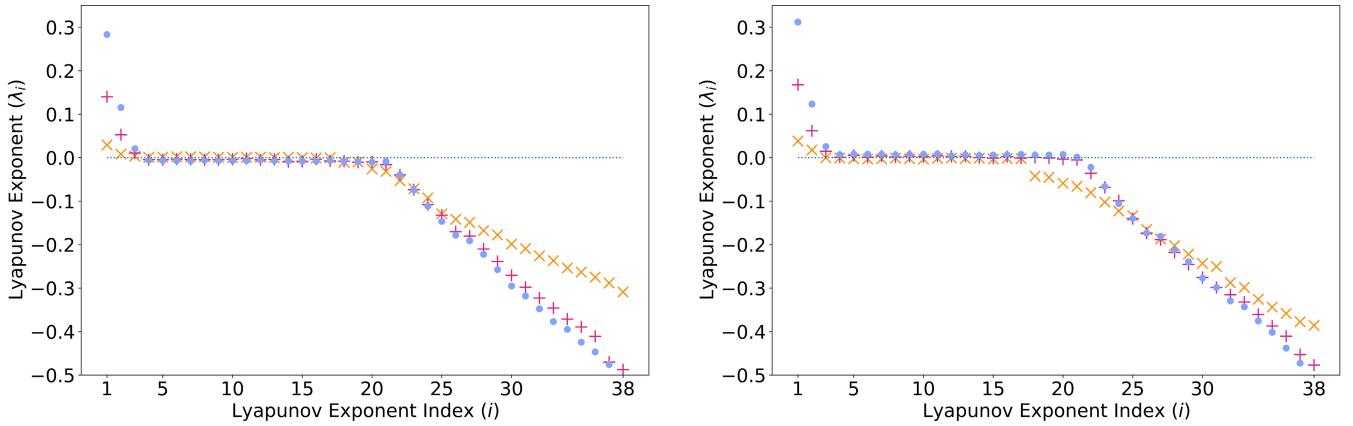

(a) Lyapunov spectra where the orange (x) attractor is shown for $C = 0.009\text{kgm}^{-2}\text{s}^{-1}$, and the other two for $C = 0.0125\text{kgm}^{-2}\text{s}^{-1}$, where $\varepsilon = 0.7$.

(b) Lyapunov spectra for $\varepsilon = 0.9$ and $C = 0.01175\text{kgm}^{-2}\text{s}^{-1}$

FIGURE 4 The Lyapunov spectra, shown in days^{-1}, for the three distinct attractors found are plotted to compare the magnitude of the largest Lyapunov exponent λ_1 and the number of near-zero Lyapunov exponents. [Colour figure can be viewed at wileyonlinelibrary.com]

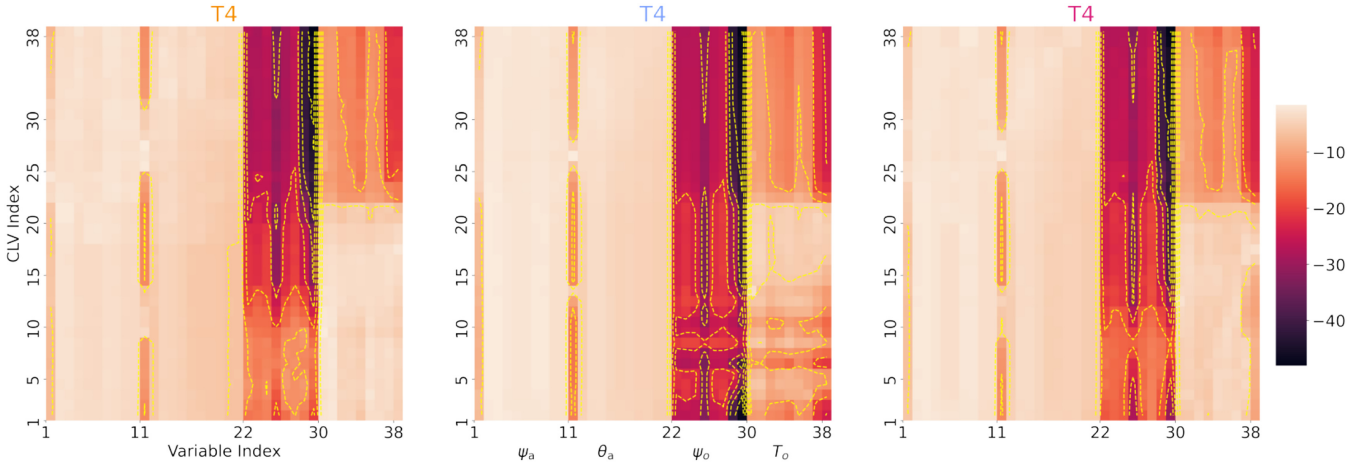

FIGURE 5 The variance of the CLVs (shown on a $\log_{10}$ scale), for each of the three distinct attractors shown in Figure 1. The attractors are designated by the colour of their title, which corresponds to the previous sections (orange on left, blue in the middle, and pink on the right). The orange (image on the left) attractor CLVs are calculated for $\varepsilon = 0.7$ and $C = 0.009\,\text{kg}\cdot\text{m}^{-2}\cdot\text{s}^{-1}$, and the CLVs for the other two attractors are calculated with $\varepsilon = 0.7$ and $C = 0.0125\,\text{kg}\cdot\text{m}^{-2}\cdot\text{s}^{-1}$. [Colour figure can be viewed at wileyonlinelibrary.com]

model variables on the x-axis. The variables are ordered as follows:

- atmospheric barotropic stream functions ψ_a (index: 1–10);
- atmospheric baroclinic stream functions θ_a (index: 11–21);
- ocean barotropic stream functions ψ_o (index: 22–29);
- ocean temperature T_o (index: 30–38).

As expected, the majority of the variance is seen in the atmosphere, as these variables are the components that contribute to the fast timescale dynamics of the system. All three attractors present coupling for CLV indices 13–22, where the ocean temperature variables present similar variability to the atmosphere variables. The near-zero Lyapunov exponents (CLV index 4–22) in general present larger variance on the ocean variables (columns 22–38). All three attractors present similar dynamics for indices greater than 22, where the ocean components have low projection on the dynamics, implying that large-magnitude negative Lyapunov exponents are caused predominantly by the atmosphere dynamics. However, the attractors that present LFV have higher variance for indices 1–12, implying that in these attractors the ocean

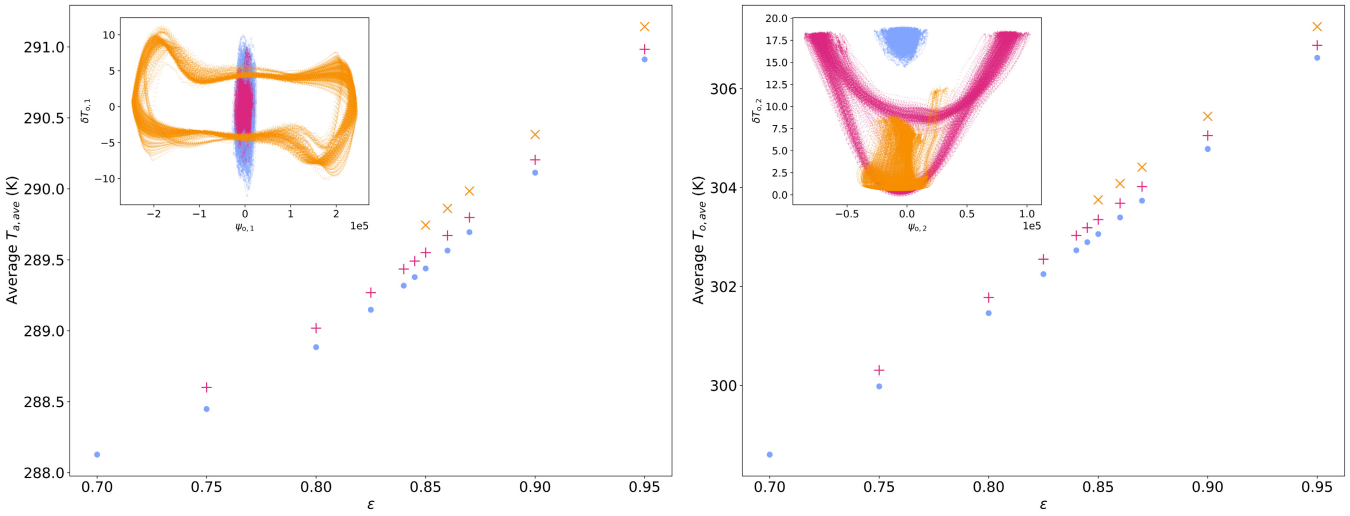

FIGURE 6 Temperature–ε diagrams showing the averaged atmosphere (left) and ocean (right) temperatures. The different colours represent stable branches that present qualitatively different attractors. Here we only present the T4 model run results, as the DE results produce the same results and the temperature differences between the three branches of the DE runs are too small to be visible on these graphs. As in Figure 1, the attractors are projected onto the plane of ocean variables with the single gyre (left) and double gyre (right) for $\varepsilon = 0.9$. [Colour figure can be viewed at wileyonlinelibrary.com]

temperature has a stabilising impact on the atmosphere dynamics and that there is a greater level of coupling between ocean and atmosphere. In addition, the orange attractor (heat map on the left-hand side) shows greater coupling between all four components of the model, as the ocean stream functions show higher variance for indices 1–10. This explains the low magnitude of the positive Lyapunov exponents for this attractor, as the unstable atmosphere components present high levels of coupling with the stable ocean.

3.2 | Emissivity

To simulate the impact of climate change on the ocean–atmosphere dynamics in the MAOOAM model, the emissivity ε is increased. Rising the emissivity acts as a proxy for rising levels of greenhouse gases, causing the atmosphere to 'trap' a larger proportion of the outgoing longwave radiation, thus increasing the average ocean and atmosphere temperatures. We picked a single value of ocean–atmosphere coupling $C = 0.01175\,\mathrm{kg}\cdot\mathrm{m}^{-2}\cdot\mathrm{s}^{-1}$ to investigate. In the previous section, this value of C resulted in a single stable attractor, for $\varepsilon = 0.7$.

3.2.1 | Multistabilities in temperature–ε

By using temperature–ε diagrams, shown in Figure 6, which present the average spatial and temporal temperatures of stable attractors found numerically, we can see that as the emissivity increases bifurcations occur at two values, leading to an additional two attracting branches. We have coloured the attracting branches to display the attractors that present qualitatively distinct behaviour. On these images we only present the results from the T4 model runs, as each of the T4 and DE model runs presented similar trajectory behaviour, but the resulting average temperatures of the three distinct branches in the DE runs were too close to be visible on the graph. This is because of the higher order nonlinear terms being removed in the linearised version, as explained in Section 3.1.2.

We have taken the three attractors that we found at $\varepsilon = 0.9$ and projected these onto the planes $(\psi_{o,1}, T_{o,1})$ and $(\psi_{o,2}, T_{o,2})$, and these are also shown in Figure 6. We can see that two of the attractors (shown in pink (+) and blue (dots)) present the same behaviour as seen in Section 3.1; in addition, the highest temperature branch (shown in orange) appears qualitativelyto have similarities with the attractor that showed a periodic behaviour with respect to $(\psi_{o,1}, T_{o,1})$ that we also saw in the previous section. Therefore, increasing the value of ε appears to have the impact of providing stability to unstable branches. Figure 6 shows that the average temperatures in the atmosphere and ocean rise quickly as ε is increased, but in addition there are multistabilities that are separated by up to 1 K for the same emissivity values.

As in Section 3.1, we visualise the level of ocean–atmosphere coupling by projecting the three attractors onto the first atmosphere mode and the single and double gyre ocean modes, as shown in Figure 7.

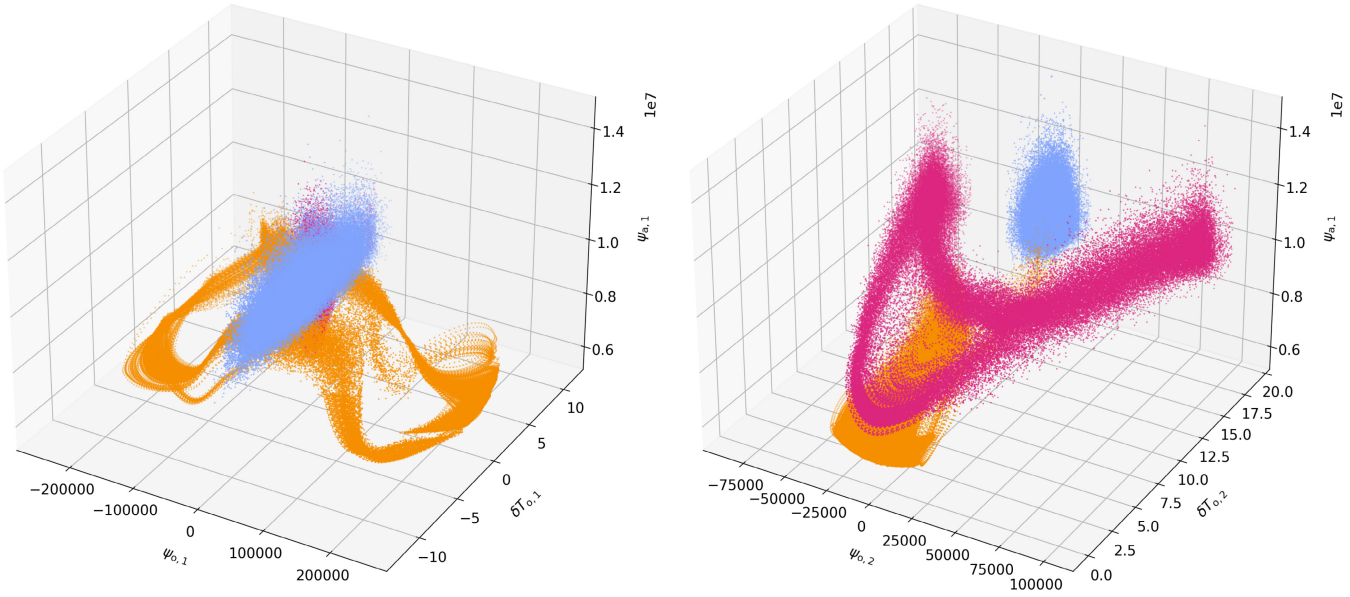

FIGURE 7 The three distinct attractors found at $C = 0.01175\,\mathrm{kg}\cdot\mathrm{m}^{-2}\cdot\mathrm{s}^{-1}$ and $\varepsilon = 0.9$ are projected onto $(\psi_{a,1}, \psi_{o,1}, T_{o,1})$ and $(\psi_{a,1}, \psi_{o,2}, T_{o,2})$, left and right respectively. The attractors are coloured to match the diagrams shown in Figure 6. [Colour figure can be viewed at wileyonlinelibrary.com]

As with the previous section, we see that the orange attractor displays an oscillatory behaviour, coupling the barotropic stream functions and the single gyre variables, and the pink attractor displays LFV with the double gyre variables. Again, we see two distinct flows where coupling exists between the ocean and atmosphere, over decadal time periods. These results show that, in the MAOOAM model, rising emissivity leads to multistabilities in the ocean–atmosphere system, which were not present at low levels of emissivity. From our model runs we have not found examples of trajectories switching between the attracting branches; however, all of our model runs were undertaken using a constant solar forcing. To understand the robustness of the attractors to forcing, further model runs will have to be undertaken.

Similarly to Section 3.1.2, we have produced videos to show the resulting ocean stream function and temperature behaviour given the attractors. These videos can be found in the Supporting Information. The qualitative behaviour of each of the attractors identified in this section is similar to that of the corresponding attractors (those sharing the same colours) in Section 3.1.2. One minor difference in the results between the ocean–atmosphere coupling model runs and the emissivity model runs is that the LFV in the orange attractor over the first ocean mode $\phi_{o,1}$ is more clearly defined. This is shown by the projection of the attractor on the plane $(\psi_{o,1},\ T_{o,1})$, where the oscillating behaviour over these variables contains less noise and variation. This change in the orange attractor could be caused by the increase in ocean–atmosphere coupling between the two runs, where we used the value of $C = 0.009\,\mathrm{kg}\cdot\mathrm{m}^{-2}\cdot\mathrm{s}^{-1}$ in Section 3.1.2 and $C = 0.01175\,\mathrm{kg}\cdot\mathrm{m}^{-2}\cdot\mathrm{s}^{-1}$ in this section.

3.2.2 | Lyapunov stability–ε

Following the format of Section 3.1.3, we present the LLEs in Figure 3b, where ε is varied, and we fix the ocean–atmosphere coupling at $C = 0.01175\,\mathrm{kg}\cdot\mathrm{m}^{-2}\cdot\mathrm{s}^{-1}$. As the value of ε is increased we see additional attractors appear; however, the value of the LLEs on each attracting branch does not alter with emissivity. This is because the emissivity has the impact of increasing the temperature of the layers evenly in space. The atmospheric layers in the model are driven from the meridional gradient in solar insolation, leading to baroclinic instability. In the current model setup, the emissivity has no impact on this temperature gradient. To model the expected outcomes of global heating more closely, model runs should be undertaken where the rising emissivity reduces the temperature gradient between the Arctic and the Equator (Francis and Vavrus, 2012; Rantanen *et al.*, 2022).

We have presented the Lyapunov spectra of the three attractors at $\varepsilon = 0.9$, for $C = 0.01175\,\mathrm{kg}\cdot\mathrm{m}^{-2}\cdot\mathrm{s}^{-1}$ in Figure 4b. Interestingly, the orange attractor, with the lowest magnitude LLE, shows a significantly lower number of near-zero Lyapunov exponents compared with the other two attractors and also the orange attractor presented in Section 3.1.3. There is a clear drop in the magnitude of the Lyapunov exponents at index 18. This is an interesting result, as it implies that the Lyapunov dimension of

this attractor is significantly lower than that of the other attractors. This difference between the Lyapunov spectra of the orange attractors in Figure 4a,b could be caused by the increase in ocean–atmosphere coupling between the two model runs, from $C = 0.009\,\mathrm{kg}\cdot\mathrm{m}^{-2}\cdot\mathrm{s}^{-1}$ to $C = 0.0175\,\mathrm{kg}\cdot\mathrm{m}^{-2}\cdot\mathrm{s}^{-1}$ in this section.

3.3 | Impact of model resolution

We investigated the impact of the model resolution on the results presented. The truncation (measured as the number of periods of a sine wave over the basin $x \in [0, 2\pi/n]$, $y \in [0, \pi]$) of the model was influenced by previous work using the MAOOAM model, which was set at (2×2) in the atmosphere and (2×4) in the ocean. This truncation in the atmosphere matches Reinhold and Pierrehumbert (1982), and the ocean truncation was chosen to match the number of atmosphere modes more closely and provide a more realistic ocean temperature profile (Vannitsem, 2015). As the number of modes used increases, the model resolution increases. However, as shown by Cehelsky and Tung (1987), for such models the accuracy is dependent on including certain modes that interact nonlinearly, which are inherent in the full system and not necessarily dependent on the model resolution.

To test the impact of model resolution on the attractors, we have run the DE model for key parameter values that we identified in the previous sections. The DE rather than T4 model was used, as the quartic term would result in model runs that take a long time. Following the work of Cehelsky and Tung (1987), we have run the model at resolutions of (4×4) and (6×6) in both the ocean and the atmosphere. In addition, the (6×6) resolution model has approximately the same scale as the Rhines scale (defined as $\sqrt{U/\beta}$, where U is the flow velocity and β is the gradient of the Coriolis parameter) in the model atmosphere, which marks the transition from wave-dominated to turbulent dynamics (Rhines, 1975) and thus provides a resolution where we would expect the turbulent dynamics to impact the solutions. However, due to the order-of-magnitude difference between flow velocities in the ocean and atmosphere, the Rhines scale in the ocean is approximately an order of magnitude smaller than that in the atmosphere, and as a result would require an ocean resolution of $\sim (60 \times 60)$, which would be computationally very expensive at this stage.

We ran higher resolution runs for $C = 0.009$ and $C = 0.0125$ while fixing $\epsilon = 0.7$, to compare the results with those in Section 3.1. We found that the multistability for $C = 0.009$ collapsed into a single attractor, however we could still find two distinct attractors for $C = 0.0125$ (shown in Figure 8c). These results are shown in Figure 8a–d. The results here are similar to those of De Cruz *et al.* (2016), where the LFV, while persisting, becomes less pronounced as the model resolution increases. Another very interesting result of the 6×6 formulation is that the range of values of the variable $\psi_{o,2}$ are now mostly positive, suggesting that the structure of the double gyres shows stronger similarities with the double gyres found in the North Atlantic basin.

We also ran higher resolution models for $\epsilon = 0.9$ and $C = 0.01175$, for comparison with the results shown in Section 3.2. For both the (4×4) and (6×6) resolution runs, the multiple attractors were no longer stable and we found a single attractor. These results are shown in Figure 8e,f.

The higher resolution runs show that these novel attractors found are dependent on the model resolution and specific nonlinear interactions between the spectral modes. These results are in line with the results of Cehelsky and Tung (1987), who found that the multiple regime behaviour of the baroclinic model disappeared at higher resolutions. In our work, however, we do find that multistability persists for certain atmosphere–ocean couplings at (4×4) resolution. Further studies are needed to investigate the values of coupling for which this multistability exists, to investigate the impact of the full quartic temperature term and also the nature of the LFV emerging in a systematic way.

4 | DISCUSSION

We have described the novel multistabilities found in a reduced-order atmosphere–ocean model, resulting from not linearising the longwave radiation terms. The modifications made to the MAOOAM model have resulted in several features that were not present in the original linearised version with fixed reference temperature. This study introduced two new versions of the model (the dynamic equilibria and nonlinear versions), and compared the results of these versions with the existing linear model. The properties of the new attractor found, as well as the region of multistability, were analysed qualitatively and by using the Lyapunov properties of the attractors.

We have demonstrated in the reduced-order ocean–atmosphere model, MAOOAM, that by modifying the linearisation of the longwave radiation terms we can obtain three qualitatively distinct attractors, with intervals of multistability for certain parameters. Interestingly, the dynamic equilibria version of the model, which includes the same linearisation as the original model but allows the zeroth-order equilibrium temperature to change with time, presents similar dynamics to the fully nonlinear version for most parameter values. All three distinct attractors can be obtained in the dynamic

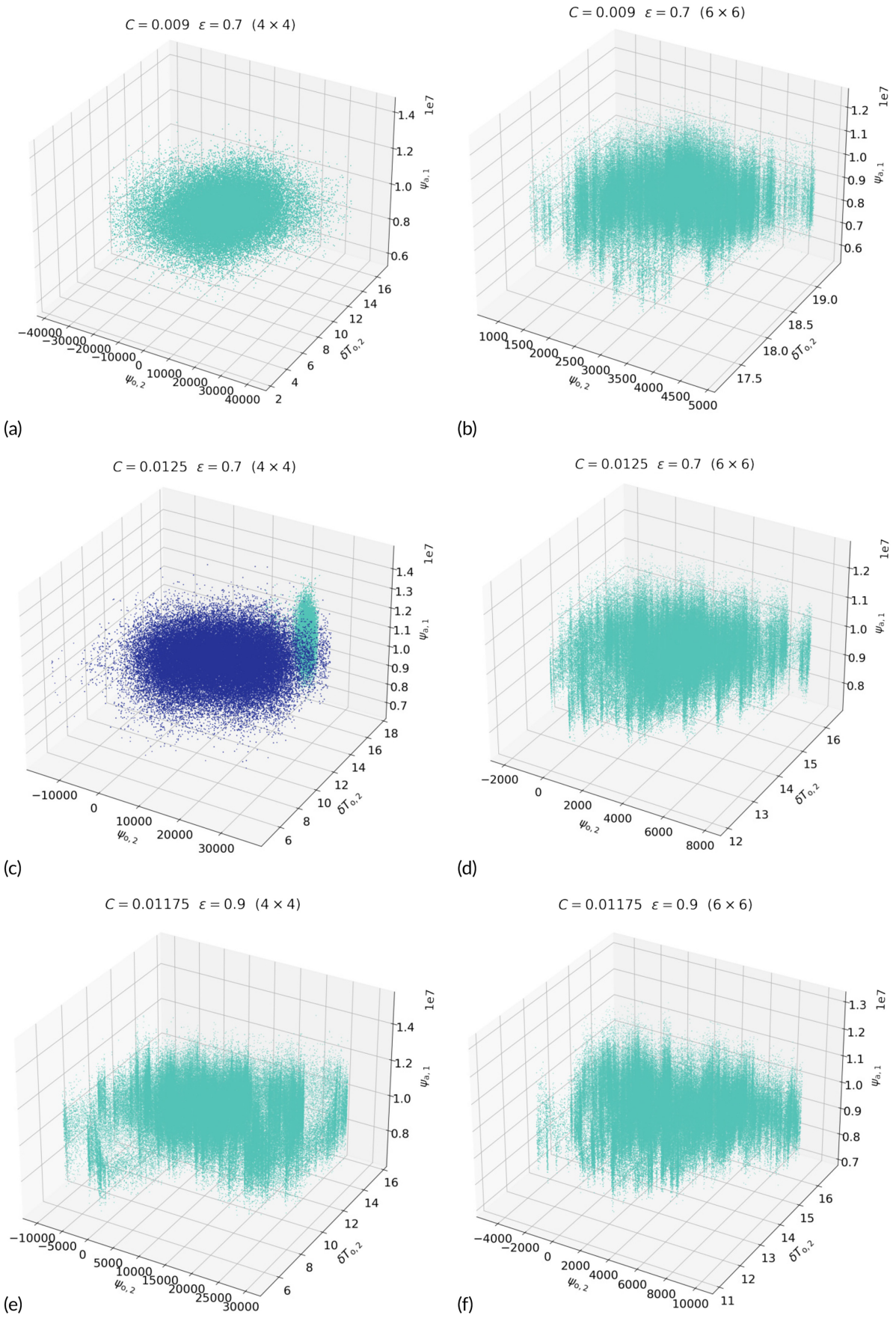

FIGURE 8 High-resolution model runs. [Colour figure can be viewed at wileyonlinelibrary.com]

equilibria (DE) version, where there are two attractors that present LFV while representing largely different coupled ocean–atmosphere flows. In addition, the DE version of the model can be run in the same length of time as the fixed reference temperature version, which is almost an order of magnitude faster than the nonlinear version of the model.

Two of the distinct attractors present LFV behaviour. One of the attractors, which displays LFV over the second ocean mode ϕ_2, has been identified in the linear model. In this study we found an additional attractor that displays LFV over the first ocean mode ϕ_1, which has not been identified in the linear model. This attractor has a longer timescale ($\sim$ 80–100 years) compared with the first attractor (which displays a timescale of approximately 70 years). In addition the two attractors display marked differences in the ocean and atmosphere flows, with one attractor producing double gyre behaviour, similar to that observed over the North Atlantic, and the other attractor displaying a more complex flow, where the main relationships are with the first ocean mode ϕ_1 and the fifth ocean mode ϕ_5. This attractor displayed the greatest degree of coupling between the ocean and atmosphere compared with the other attractors, where all four variables are coupled. This leads to significantly lower positive Lyapunov exponents, which implies that this attractor would have a longer forecasting window. Further studies will need to be done to find whether this attractor describes a real-world ocean–atmosphere flow.

The DE version of the model was run at higher model resolutions and it was found that these novel attractors were no longer attracting for different model resolutions. However a multistability persisted for some parameter values, and others showed a tendency for a stable positive double gyre system. Further studies are required to investigate what type of solutions could emerge by changing the bifurcation parameters in a systematic way, and to explore whether other parameter ranges are needed to see the development of multistability.

A key reason for undertaking this study and not linearising the longwave radiation terms was to investigate the potential of tipping between multistabilities. While we found cases of distinct attractors for the same parameter values, we could not produce trajectories that switched intermittently between the attracting branches, though it is not possible to rule out the possibility of such trajectories existing. However, in the current model setup all external forcings are constant with respect to time. To test the robustness of the stability of each attractor, model runs could be undertaken where stochastic forcing or perturbations are included, to see if there is the potential for noise-induced tipping between the attracting branches. Another potential source of tipping could come from periodic cycles, such as the annual solar cycle as implemented in a similar linearised model (Vannitsem, 2017).

With rising global temperatures, investigating the possibility and impact of tipping points in the climate is of great importance. Understanding how rising temperatures could impact existing multidecadal patterns in the climate could lead to a better understanding of how established climate patterns may look in the future, or whether there is the possibility of abrupt transitions from one regime to another. This article has introduced a modified model that produces multistabilities, as well as attractors that present LFV, which become stable for rising emissivity. These properties are of interest, as they facilitate the study of attractors that allow forecasting well beyond the atmospheric Lyapunov time, as well as the potential of tipping from one attractor to the other. These aspects will be investigated in the future.

AUTHOR CONTRIBUTIONS

Oisín Hamilton: data curation; investigation; project administration; visualization; writing – original draft; writing – review and editing. **Jonathan Demaeyer:** formal analysis; software; supervision; validation; writing – review and editing. **Stéphane Vannitsem:** funding acquisition; supervision; visualization; writing – review and editing. **Michel Crucifix:** supervision; writing – review and editing.

ACKNOWLEDGEMENTS

This project has received funding from the European Union's Horizon 2020 research and innovation programme under the Marie Sklodowska–Curie grant agreement no. 956170. Michel Crucifix was funded as Research Director with the Belgian National Fund of Scientific Research.

CONFLICT OF INTEREST STATEMENT

The authors declare no conflict of interest.

DATA AVAILABILITY STATEMENT

The code used to obtain the results is a new version (v0.2.6) of qgs (Demaeyer *et al.*, 2020) that was recently released on GitHub (https://github.com/Climdyn/qgs) and Zenodo (DemaeyerDemaeyer *et al.*, 2022).

ORCID

Oisín Hamilton https://orcid.org/0000-0002-0447-1657
Jonathan Demaeyer https://orcid.org/0000-0002-5098-404X
Stéphane Vannitsem https://orcid.org/0000-0002-1734-1042
Michel Crucifix https://orcid.org/0000-0002-3437-4911

REFERENCES

Armstrong McKay, D.I., Staal, A., Abrams, J.F., Winkelmann, R., Sakschewski, B., Loriani, S., Fetzer, I., Cornell, S.E., Rockström, J. and Lenton, T.M. (2022) Exceeding 1.5 °C global warming could trigger multiple climate tipping points. *Science*, 377, eabn7950.

Årthun, M., Wills, R.C.J., Johnson, H.L., Chafik, L. and Langehaug, H.R. (2021) Mechanisms of decadal North Atlantic climate variability and implications for the recent cold anomaly. *Journal of Climate*, 34, 19.

Barsugli, J.J. and Battisti, D.S. (1998) The basic effects of atmosphere–ocean thermal coupling on midlatitude variability. *Journal of the Atmospheric Sciences*, 55, 17.

Berloff, P., Dewar, W., Kravtsov, S. and McWilliams, J. (2007) Ocean Eddy dynamics in a coupled ocean–atmosphere model. *Journal of Physical Oceanography*, 37, 1103–1121.

Cehelsky, P. and Tung, K.K. (1987) Theories of multiple equilibria and weather regimes—a critical reexamination. Part II: Baroclinic two-layer models. *Journal of the Atmospheric Sciences*, 44, 3282–3303.

Cessi, P. (2000) Thermal feedback on wind stress as a contributing cause of climate variability. *Journal of Climate*, 13, 232–244.

Charney, J.G. and DeVore, J.G. (1979) Multiple flow equilibria in the atmosphere and blocking. *Journal of Atmospheric Sciences*, 36, 1205–1216.

Charney, J.G. and Straus, D.M. (1980) Form-drag instability, multiple equilibria and propagating planetary waves in baroclinic, orographically forced, planetary wave systems. *Journal of Atmospheric Sciences*, 37, 1157–1176.

Chen, L.G. and Dewar, W.K. (1993) Intergyre communication in a three-layer model. *Journal of Physical Oceanography*, 23, 855–878.

Czaja, A. and Marshall, J. (2001) Observations of atmosphere-ocean coupling in the North Atlantic. *Quarterly Journal of the Royal Meteorological Society*, 127, 1893–1916.

De Cruz, L., Demaeyer, J. and Vannitsem, S. (2016) The modular arbitrary-Order Ocean-atmosphere model: MAOOAM v1.0. *Geoscientific Model Development*, 9, 2793–2808.

Demaeyer, J., De Cruz, L. and Hamilton, O. (2022) Qgs version 0.2.6 release. https://doi.org/10.5281/zenodo.7404671.

Demaeyer, J., De Cruz, L. and Vannitsem, S. (2020) Qgs: a flexible python framework of reduced-order multiscale climate models. *Journal of Open Source Software*, 5, 2597.

Dewar, W.K. (2001) On ocean dynamics in midlatitude climate. *Journal of Climate*, 14, 4380–4397.

Egger, J. (1978) Dynamics of blocking highs. *Journal of the Atmospheric Sciences*, 35, 1788–1801.

Ferreira, D., Frankignoul, C. and Marshall, J. (2001) Coupled ocean–atmosphere dynamics in a simple midlatitude climate model. *Journal of Climate*, 14, 3704–3723.

Francis, J.A. and Vavrus, S.J. (2012) Evidence linking Arctic amplification to extreme weather in mid-latitudes. *Geophysical Research Letters*, 39. https://doi.org/10.1029/2012GL051000

Goodman, J. and Marshall, J. (1999) A model of decadal middle-latitude atmosphere–ocean coupled modes. *Journal of Climate*, 12, 621–641.

Hogg, A.M.C., Dewar, W.K., Killworth, P.D. and Blundell, J.R. (2003) A quasi-geostrophic coupled model (Q-GCM). *Monthly Weather Review*, 131, 2261–2278.

Hogg, A.M.C., Dewar, W.K., Killworth, P.D. and Blundell, J.R. (2006) Decadal variability of the midlatitude climate system driven by the ocean circulation. *Journal of Climate*, 19, 1149–1166.

Holton, J.R. (2004) *An Introduction to Dynamic Meteorology*, 4th edition. International Geophysics Series. Vol. 88. Cambridge, MA: Elsevier Academic Press.

Houghton, J. (1986) *The Physics of the Atmospheres*, 2nd edition. Cambridge: Cambridge University Press.

Hurrell, J.W., Kushnir, Y., Ottersen, G. and Visbeck, M. (Eds.) (2003) An overview of the North Atlantic oscillation. In: *The North Atlantic Oscillation: Climatic Significance and Environmental Impact*. Geophysical Monograph Series, Vol. 134. Washington, DC: American Geophysical Union, pp. 1–35.

Itoh, H. and Kimoto, M. (1996) Multiple attractors and chaotic itinerancy in a Quasigeostrophic model with realistic topography: implications for weather regimes and low-frequency variability. *Journal of the Atmospheric Sciences*, 53, 2217–2231.

Kravtsov, S., Berloff, P., Dewar, W.K., Ghil, M. and McWilliams, J.C. (2006) Dynamical origin of low-frequency variability in a highly nonlinear midlatitude coupled model. *Journal of Climate*, 19, 6391–6408.

Kravtsov, S. and Robertson, A. (2002) Midlatitude Ocean-atmosphere interaction in an idealized coupled model. *Climate Dynamics*, 19, 693–711.

Kuptsov, P.V. and Parlitz, U. (2012) Theory and computation of covariant Lyapunov vectors. *Journal of Nonlinear Science*, 22, 727–762.

Legras, B. and Ghil, M. (1985) Persistent anomalies, blocking and variations in atmospheric predictability. *Journal of the Atmospheric Sciences*, 42, 433–471.

Lenton, T.M., Held, H., Kriegler, E., Hall, J.W., Lucht, W., Rahmstorf, S. and Schellnhuber, H.J. (2008) Tipping elements in the Earth's climate system. *Proceedings of the National Academy of Sciences*, 105, 1786–1793.

Lorenz, E.N. (1963) The mechanics of vacillation. *Journal of the Atmospheric Sciences*, 20, 448–465.

Lorenz, E.N. (1969) The predictability of a flow which possesses many scales of motion. *Tellus*, 21, 289–307.

Lorenz, E.N. (1982) Atmospheric predictability experiments with a large numerical model. *Tellus*, 34, 505–513.

Lorenz, E.N. (1984) Irregularity: a fundamental property of the atmosphere. *Tellus A*, 36A, 98–110.

Nauw, J.J. and Dijkstra, H.A. (2001) The origin of low-frequency variability of double-gyre wind-driven flows. *Journal of Marine Research*, 59, 567–597.

Nese, J.M. and Dutton, J.A. (1993) Quantifying predictability variations in a low-order ocean-atmosphere model: a dynamical systems approach. *Journal of Climate*, 6, 185–204.

Pierini, S. (2011) Low-frequency variability, coherence resonance, and phase selection in a low-order model of the wind-driven ocean circulation. *Journal of Physical Oceanography*, 41, 1585–1604.

Rantanen, M., Karpechko, A.Y., Lipponen, A., Nordling, K., Hyvärinen, O., Ruosteenoja, K., Vihma, T. and Laaksonen, A. (2022) The Arctic has warmed nearly four times faster than the globe since 1979. *Communications Earth & Environment*, 3, 168.

Reinhold, B.B. and Pierrehumbert, R.T. (1982) Dynamics of weather regimes: quasi-stationary waves and blocking. *Monthly Weather Review*, 110, 1105–1145.

Rhines, P.B. (1975) Waves and turbulence on a beta-plane. *Journal of Fluid Mechanics*, 69, 417–443.

Saravanan, R. and Mc Williams, J.C. (1995) Multiple equilibria, natural variability, and climate transitions in an idealized ocean–atmosphere model. *Journal of Climate*, 8, 2296–2323.

Spydell, M. and Cessi, P. (2003) Baroclinic modes in a two-layer basin. *Journal of Physical Oceanography*, 33, 610–622.

Steffen, W., Rockström, J., Richardson, K., Lenton, T.M., Folke, C., Liverman, D., Summerhayes, C.P., Barnosky, A.D., Cornell, S.E., Crucifix, M., Donges, J.F., Fetzer, I., Lade, S.J., Scheffer, M., Winkelmann, R. and Schellnhuber, H.J. (2018) Trajectories of the earth system in the anthropocene. *Proceedings of the National Academy of Sciences*, 115, 8252–8259.

van der Avoird, E., Dijkstra, H., Nauw, J. and Schuurmans, C. (2002) Nonlinearly induced low-frequency variability in a midlatitude coupled ocean-atmosphere model of intermediate complexity. *Climate Dynamics*, 19, 303–320.

Vannitsem, S. (2015) The role of the ocean mixed layer on the development of the North Atlantic oscillation: a dynamical system's perspective. *Geophysical Research Letters*, 42, 8615–8623.

Vannitsem, S. (2017) Predictability of large-scale atmospheric motions: Lyapunov exponents and error dynamics. *Chaos: An Interdisciplinary Journal of Nonlinear Science*, 27, 032101.

Vannitsem, S. and De Cruz, L. (2014) A 24-variable low-order coupled ocean–atmosphere model: OA-QG-WS v2. *Geoscientific Model Development*, 7, 649–662.

Vannitsem, S., Demaeyer, J., De Cruz, L. and Ghil, M. (2015) Low-frequency variability and heat transport in a low-order nonlinear coupled ocean–atmosphere model. *Physica D: Nonlinear Phenomena*, 309, 71–85.

Vannitsem, S. and Duan, W. (2020) On the use of near-neutral backward Lyapunov vectors to get reliable ensemble forecasts in coupled ocean– atmosphere systems. *Climate Dynamics*, 55, 1125–1139.

Vannitsem, S. and Lucarini, V. (2016) Statistical and dynamical properties of covariant Lyapunov vectors in a coupled atmosphere-ocean model-multiscale effects, geometric degeneracy, and error dynamics. *Journal of Physics A: Mathematical and Theoretical*, 49, 224001.

Vannitsem, S., Solé-Pomies, R. and De Cruz, L. (2019) Routes to long-term atmospheric predictability in reduced-order coupled ocean– atmosphere systems: impact of the ocean basin boundary conditions. *Quarterly Journal of the Royal Meteorological Society*, 145, 2791–2805.

Veronis, G. (1963) An analysis of wind-driven ocean circulation with a limited number of Fourier components. *Journal of the Atmospheric Sciences*, 20, 577–593.

Weng, W. and Neelin, J.D. (1998) On the role of ocean-atmosphere interaction in midlatitude interdecadal variability. *Geophysical Research Letters*, 25, 167–170.

Wu, L. and Liu, Z. (2005) North Atlantic decadal variability: Air–Sea coupling, oceanic memory, and potential northern hemisphere resonance. *Journal of Climate*, 18, 331–349.

SUPPORTING INFORMATION

Additional supporting information can be found online in the Supporting Information section at the end of this article.

How to cite this article: Hamilton, O., Demaeyer, J., Vannitsem, S. & Crucifix, M. (2023) Multistability in a coupled ocean–atmosphere reduced-order model: Nonlinear temperature equations. *Quarterly Journal of the Royal Meteorological Society*, 149(757), 3423–3439. Available from: https://doi.org/10.1002/qj.4564